Field Distribution and Coupling Investigation of an Eight-Channel RF Coil Consisting of Different Dipole Coil Elements for 7 T MRI

Zhichao Chen*, *Student Member, IEEE*, Klaus Solbach, Daniel Erni, *Member, IEEE*, and Andreas Rennings, *Member, IEEE*

***Abstract*—In this contribution, we investigate the B_1 distribution and coupling characteristics of a multichannel radio frequency (RF) coil consisting of different dipole coil elements for 7 T MRI, and explore the feasibility to achieve a compromise between field distribution and decoupling by combining different coil elements. Two types of dipole elements are considered here: the meander dipole element with a chip-capacitor-based connection to the RF shield which achieves a sufficient decoupling between the neighboring elements; and the open-ended meander dipole element which exhibits a broader magnetic field distribution. By nesting the open-ended dipole elements in between the ones with end-capacitors, the B_1 distribution, in terms of field penetration depth and homogeneity, is improved in comparison to the dipole coil consisting only of the elements with end-capacitors, and at the same time, the adjacent elements are less coupled to each other in comparison to the dipole coil consisting only of the open-ended elements. The proposed approach is validated by both full-wave simulation and experimental results.**

***Index Terms*—B_1 distribution, coupling investigation, dipole coil, multichannel coil array, 7 T MRI.**

I. Introduction

OVER the past decade, ultrahigh field (UHF) imaging ($B_0 \geq 7$ T) has attracted more and more attention due to its enhanced imaging sensitivity, increased spectral resolution, and improved scan efficiency (parallel imaging techniques), etc. [1]–[6]. Associated with the aforementioned advantages, various problems and challenges occur along with the increased field strength, such as spatially inhomogeneous B_1 field, more critical specific absorption rate (SAR) issue, susceptibility effects, etc. [1]–[3], [7], [8]. Therefore, massive effort has been devoted to the development of efficient radio frequency (RF) coils, since the conventional RF coils, such as surface coils and volume coils, challenge the limits of design and performance due to the higher magnetic resonance frequencies [9]–[13]. At higher magnetic resonance frequencies, dipole coils form a promising candidate since they effectively produce propagating electromagnetic waves toward the imaging target [14].

Recently, multichannel RF coils based on several longitudinally oriented stripline elements have been successfully applied in UHF MRI [7], [15]–[20]. For such multichannel RF coils, the coupling characteristic between the adjacent elements could impact the coil performance severely, and thus, become an important parameter for the coil design. A comparison of the coupling mechanism for various dipole coil elements is presented in [21] based on the characteristic mode analysis [22]. It has been demonstrated that the dipole element with lumped-element connection to the RF shield [23] achieves a sufficient decoupling, while the element without direct connection to the RF shield exhibits a broader transverse magnetic field distribution. The meandered dipole element without direct connection to the RF shield was initially introduced in [24], where the length of the meandered dipole elements with different termination topologies was optimized to achieve a minimized SAR. In practice, a homogeneous B_1 field and a sufficient decoupling between coil elements are pursued, especially for the receive case. Hence, RF coils, which could simultaneously possess these two features, are desired.

Here, we present an investigation of the B_1 distribution and coupling characteristics of a multichannel RF coil consisting of different dipole coil elements for 7 T MRI, and explore the feasibility to achieve a compromise between field distribution and decoupling by combining two different coil elements. The considered dipole elements are symmetrically fed stripline dipoles which are terminated by a meander structure on each side. However, different terminations from the meander to the corresponding RF shield are used: first, a lumped-element connection (end-capacitor scenario); and second, in the absence of direct connection between the RF shield and the meanders (open-ended scenario). Here, we consider three different coil setups:

1) an eight-channel coil based on dipole elements with end-capacitors;
2) an eight-channel coil based on open-ended dipole elements; and
3) an eight-channel coil based on an alternating combination of the aforementioned two dipole elements.

Manuscript received April 7, 2016; revised July 20, 2016; accepted August 18, 2016. Date of publication August 25, 2016; date of current version May 15, 2017. This work was supported by the German Science Foundation (Deutsche Forschungsgemeinschaft, DFG) under Grant RE 1684/3-2. *Asterisk indicates corresponding author.*

*Z. Chen is with the Faculty of Engineering, Laboratory for General and Theoretical Electrical Engineering (ATE), University of Duisburg-Essen, Duisburg D-47048, Germany (e-mail: zhi.chen@uni-due.de).

D. Erni and A. Rennings are with the Faculty of Engineering, Laboratory for General and Theoretical Electrical Engineering (ATE), University of Duisburg-Essen.

K. Solbach is with the Faculty of Engineering, Laboratory for High Frequency Engineering, University of Duisburg-Essen.

Digital Object Identifier 10.1109/TBME.2016.2602441

The investigation is performed based on full-wave simulations, and further validated by measurements of the excited fields.

The paper is organized as follows. Section II briefly introduces the dipole elements which will be utilized to construct the different RF coils in the forthcoming section. In Sections III and IV, the B_1 distribution and coupling characteristics of multichannel RF coils consisting of different dipole coil elements are compared based on *finite difference time domain* (FDTD) full-wave simulation and experimental results. In addition to the near-field measurements, the absolute B_1^+ maps of the proposed multichannel coils with different dipole elements are acquired and compared. Finally, conclusions are given in Section V.

II. Considered Dipole Elements

In this study, we utilize a symmetrically fed dipole element which was terminated by two meanders on each side. However, different coupling scenarios to the corresponding RF shield are considered: first, the meander is connected to the RF shield through a so-called end-capacitor with the value of 1 pF [23]; and second, a field-based coupling is used where no direct connection between the RF shield and the meanders is established (open-ended). For the second case, the meander sections are covered by substrates with high dielectric constant to finetune the current distribution on the dipole [24]. In both versions (with end-capacitor and open-ended), the stripline dipole and the corresponding RF shield are printed on Rogers RO4003 substrates (25 cm $\times$ 8 cm) with a thickness of 0.5 mm, and separated by 2 cm of air.

Fig. 1 shows the absolute magnetic field in the transverse cross section of the considered dipole elements. A homogeneous flat phantom ($\epsilon_r = 45.3$, $\sigma = 0.87$ S/m) was placed 2 cm above the dipole element. The corresponding magnetic field is normalized to the square root of the accepted power and plotted in dB. The dipole element with end-capacitors reveals a loop current which flows through the stripline and the RF shield via the end-capacitors. As a result, a relative strong magnetic field below the stripline is observed [cf. Fig. 1(a)]. Without the direct connection to the RF shield, the magnetic field of the open-ended dipole element is not confined between the stripline and the RF shield, but is distributed above the stripline in a broader manner [cf. Fig. 1(b)]. The drawback of this broader field distribution is a higher coupling between adjacent elements [21]. In addition to the broader field distribution, the open-ended dipole element also exhibits a slightly stronger field penetration into the phantom compared to the case of the dipole element with end-capacitors [cf. Fig. 1(c)].

III. Field Distribution of Eight-Channel RF Coils Based on Different Dipole Elements

In this section, we compare the B_1 distribution of an eight-channel RF coil consisting of different dipole coil elements based on full-wave simulation and near-field measurement.

A. Proposed Dipole Coils

As depicted in Fig. 2, three coil setups will be considered here:

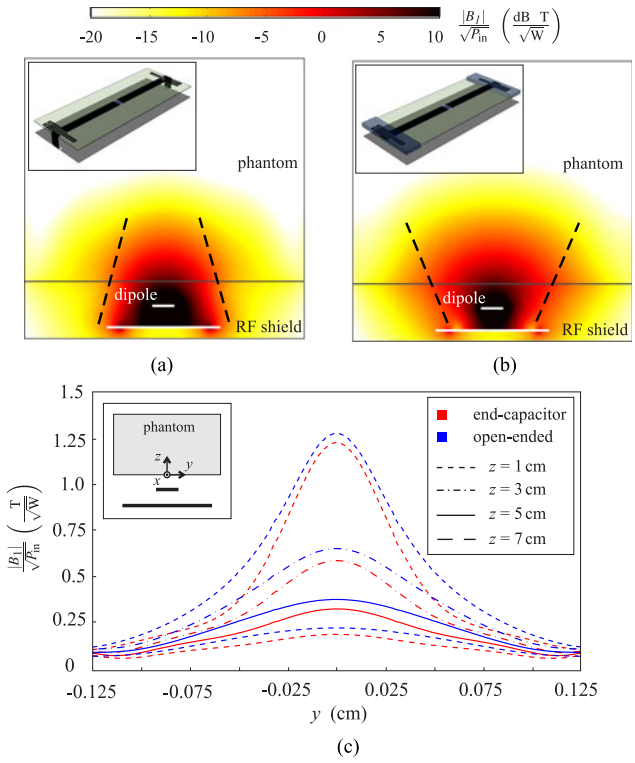

Fig. 1. Simulated absolute magnetic field distribution in the transverse cross section of the considered dipole elements: (a) dipole element with lumped element (end-capacitors) connection between the RF shield and the meander, (b) dipole element with open-ended meander terminal. The corresponding magnetic field is normalized to the square-root of the accepted power and plotted in dB. (c) The absolute $|B_1|$ distribution of the considered dipole elements along the transverse path ($x = 0$) with different penetration depth into the phantom ($z = 1, 3, 5, 7$ cm).

1) an eight-channel coil based on dipole elements with end-capacitors;
2) an eight-channel coil based on open-ended dipole elements; and
3) an eight-channel coil based on an alternate combination of the aforementioned two dipole elements.

For each case, the dipole elements are equably arranged around a cylindrical phantom ($\epsilon_r = 45.3$, $\sigma = 0.87$ S/m, $\rho = 1000$ kg/m^3) with a diameter of 20 cm. The radial separation between the coil elements and the phantom is set to 2 cm. In order to excite a circularly polarized (CP) mode, the coil elements in our case are fed equally in magnitude and with a relative phase lag of 45°.

B. Numerical Model Validation

First, the numerical models of the considered coil arrangements are validated through the comparison of full-wave simulation and experimental results.

1) Full-Wave Simulation: The transverse B_1 distributions of the proposed dipole coils are simulated with a full-wave simulator based on the FDTD method, here EMPIRE XPU,[1] and displayed in Fig. 2. For each coil setup the dipole elements are

[1]EMPIRE XPU is one of the leading three-dimensional electromagnetic field simulators. It is based on the powerful FDTD, which has become an industrial standard for RF and microwave component and antenna design.

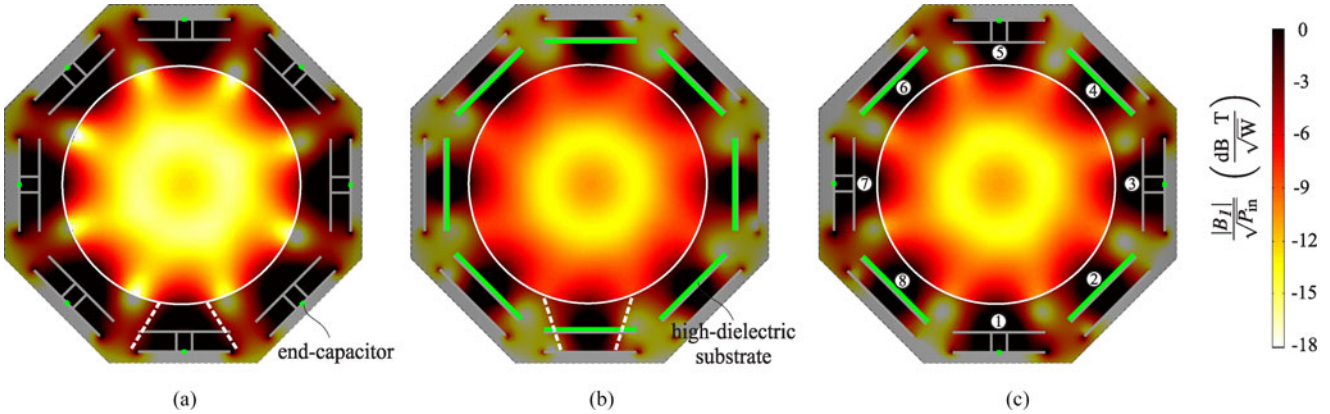

Fig. 2. Simulated $|B_1|$ distributions on the transverse cut of the proposed dipole coils: (a) an eight-channel coil based on dipole elements with end-capacitors; (b) an eight-channel coil based on open-ended dipole elements; and (c) an eight-channel coil based on an alternate combination of the aforementioned two dipole elements. The corresponding $|B_1|$ distributions are normalized to the square root of total accepted power and plotted in dB. The field distribution outside the phantom (in the shaded area) is also displayed in order to indicate the unique field pattern of different coil elements.

properly matched in such a way that the power delivered to each dipole element is identical. The corresponding field distributions are normalized to the total accepted power by the coil elements. The coil based on dipole elements with end-capacitors reveals a strong concentration of magnetic field between the stripline and the RF shield, showing a triangle-shaped field distribution, where only the tip of the triangle is extended into the phantom [cf. Fig. 2(a)]. As a result, the degradation of the B_1 field in the regions between the adjacent elements is obvious. For the coil with open-ended elements, the field is not confined below the stripline, but spread out in a broader manner inside the phantom, which results in an inverted-triangle-shaped field distribution [cf. Fig. 2(b)]. Hence, the in-between areas with low field in Fig. 2(a) are covered by the broader field distributions, and an improved B_1 homogeneity is achieved. As mentioned previously, this broader field distribution leads to a stronger coupling between the neighboring elements. Therefore, we present a new setup which achieves a compensation of the triangle- and inverted-triangle-shaped field distribution [cf. Fig. 2(c)]. In this case, the gaps between the elements with end-capacitors will be compensated by the open-ended elements, and thus, a more uniform B_1 field is observed. On the other hand, the coil will not suffer from the strong coupling between the neighboring elements, since the field generated by the elements with end-capacitors and the open-ended elements do not deeply overlap with each other as in Fig. 2(b).

Here a numerical analysis of the field parameters is performed and compared for different coils in Table I. To some extent, the averaged penetrating ability of magnetic field can be correlated to the mean value of $|B_1|$, and the homogeneity of $|B_1|$ field is then represented by the coefficient of variation (CoV) of $|B_1|$:

$$\mathrm{CoV}\left(|\mathbf{B}_1|\right) = \frac{\mathrm{std}\left(|\mathbf{B}_1|\right)}{\mathrm{mean}\left(|\mathbf{B}_1|\right)} \tag{1}$$

where std$(\cdot)$ stands for the standard deviation. A small CoV indicates a low variance of the examined variable, and thus, a better homogeneity. In comparison to the coil with end-capacitors,

TABLE I
SIMULATED FIELD PARAMETERS OF THE CONSIDERED DIPOLE COILS

Type of Coil	mean$\left(\frac{\lvert B_1\rvert}{\sqrt{P_{\mathrm{in}}}}\right)$	CoV$\left(\frac{\lvert B_1\rvert}{\sqrt{P_{\mathrm{in}}}}\right)$
CASE 1: End-Capacitor Element	0.334 $\left[\frac{\mu\mathrm{T}}{\sqrt{\mathrm{W/kg}}}\right]$	0.479
CASE 2: Open-Ended Element	0.415 $\left[\frac{\mu\mathrm{T}}{\sqrt{\mathrm{W/kg}}}\right]$	0.321
CASE 3: Combination of 1 and 2	0.398 $\left[\frac{\mu\mathrm{T}}{\sqrt{\mathrm{W/kg}}}\right]$	0.369

due to the better radiation ability the open-ended dipole element provides a better B_1 field (larger mean$(|B_1|)$ and smaller CoV$(|B_1|)$. The field parameters of the coil with combined dipole elements fall between the other two cases. Compared to the coil with end-capacitors, the combined dipole arrangement exhibits an increment of 19% on mean$(|B_1|)$, and a reduction of 23% on CoV$(|B_1|)$.

2) Experimental Results: Besides the FDTD full-wave simulation, the magnetic field distributions of different coil setups are also investigated by near-field measurement. The experimental setup for near-field measurement is depicted in Fig. 3. The dipole elements are equably arranged around a cylindrical phantom ($\epsilon_r \approx 45.3$, $\sigma \approx 0.87$ S/m) with a diameter of 20.5 cm. Fig. 3 displays the particular case with combined coil elements, it should be noted that the other two cases share the same measurement setup. The geometry parameters of the coil elements are in accordance with the ones utilized in simulation. The source power is first split into four equal parts with a 90° phase-shift using a Butler matrix. Each output signal is followed by a subsequent power amplifier and a Wilkinson power divider, which provides an additional 45° phase-shift between the two outputs. In total, eight equal signals with a relative phase lag of 45° are generated and applied to the dipole elements. In our case, the power accepted for each channel is roughly 5 W, and varies a

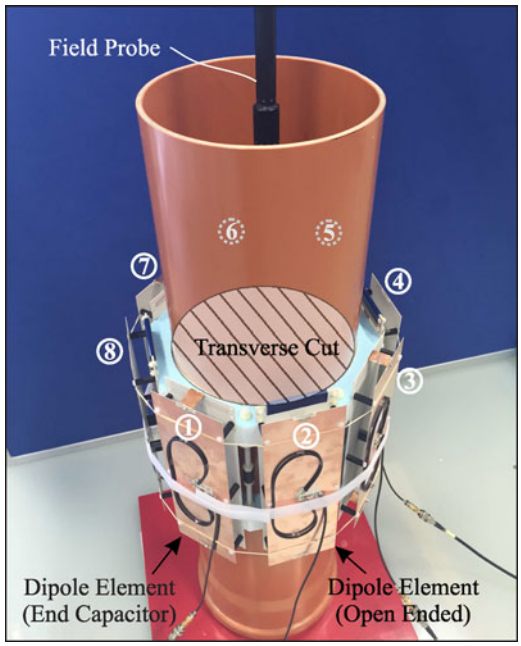

Fig. 3. Experimental setup for near-field measurement. The dipole elements are equably arranged around a cylindrical phantom ($\epsilon_r \approx 45.3$, $\sigma \approx 0.87$ S/m) with a diameter of 20 cm.

little bit between elements due to the slightly different matching behaviors.

Fig. 4 shows the measured absolute magnetic field distribution on the transverse cut inside the phantom (cf. Fig. 3) for different dipole coils. The corresponding field distributions are normalized to the square root of the total accepted power by the coil elements. The slight asymmetry of the field pattern is mainly caused by the unequal excitation of the coil elements due to the imperfect power splitting by the Bulter matrix and the power dividers. Besides, the coil misalignment and slightly different matching levels between coil elements could also aggravate the asymmetry. Due to the finite thickness of the side wall of the phantom container and the radius of the field probe, the measurable field region ($D = 16$ cm) is smaller than the actual cross section of the phantom ($D = 20$ cm). This smaller field of view (FoV) weakens the difference on field distribution between the dipole coils under comparison, since in the outer region of the phantom the field difference is more prominent. Nevertheless, the coil with open-ended elements reveals the most promising $|B_1|$ distribution, in terms of mean value and CoV of $|B_1|$. Compared to the case with end-capacitors, the combination of two different dipole elements exhibits a more homogeneous and strengthened $|B_1|$ distribution, especially in the regions between the neighboring elements.

Similarly, a numerical analysis of the field parameters is carried out based on the measured data (cf. Table II). In general, the field parameters of the measured magnetic field shows the same tendency as the ones based on full-wave simulation in Table I. The coil with open-ended dipole elements reveals the largest mean value and the smallest CoV of the absolute magnetic field, indicating an improved field distribution. The coil

TABLE II
MEASURED FIELD PARAMETERS OF THE CONSIDERED DIPOLE COILS

Type of Coil	mean$\left(\frac{\lvert B_1\rvert}{\sqrt{P_{\text{in}}}}\right)$	CoV$\left(\frac{\lvert B_1\rvert}{\sqrt{P_{\text{in}}}}\right)$
CASE 1: End-Capacitor Element	0.143 $\left[\frac{\mu\text{T}}{\sqrt{\text{W/kg}}}\right]$	0.574
CASE 2: Open-Ended Element	0.186 $\left[\frac{\mu\text{T}}{\sqrt{\text{W/kg}}}\right]$	0.548
CASE 3: Combination of 1 and 2	0.159 $\left[\frac{\mu\text{T}}{\sqrt{\text{W/kg}}}\right]$	0.566

with end-capacitors exhibits a comparatively inferior field distribution, denoted by the smallest mean value and the largest CoV of the absolute magnetic field. The field parameters of the coil with combined dipole elements again fall in between the other two cases, suggesting an intermediate magnetic field distribution. Since the accessible field region for measurement is smaller than the phantom cross section in full-wave model (due to the sidewall of the phantom container and the diameter of the field probe), the measured field magnitude is smaller than the simulation results [cf. Fig. 2(a)–(c)]. As mentioned earlier, this smaller FoV weakens the difference on field distribution between the three compared coil arrangements and leads to a less different CoV in Table II. We can notice that due to the smaller mean values, the CoV of the measured magnetic field in Table II are larger than the ones computed based on the simulation results (cf. Table I).

Basically, the full-wave simulation and near-field measurement reveal a very similar magnetic field distribution inside the phantom, which is also confirmed by the numerical analysis. Through the comparison of simulated and measured results, the numerical models of the considered coil arrangements are effectively validated.

C. B_1^+ Distribution

For a multichannel RF coil, the CP magnetic field, namely the B_1^+ field, inside the phantom is mostly considered [25], [26]. In our case the coil elements are fed equally in magnitude and with a relative phase lag of 45° to excite the first-order CP+ mode. For the UHF MRI application, the local peak SAR is a critical limitation which should be minimized. In addition to the absolute field distribution, here we also investigate the CP B_1^+ field inside the phantom, and normalize it to the square root of peak SAR (cf. Fig. 5). In general, the $|B_1^+|$ distributions show a similar tendency as the absolute B_1 distribution in Fig. 2, except for the slightly rotated field patterns due to the circular polarization.

The numerical analysis of the $|B_1^+|$ distribution in Table III reveals a similar tendency as the $|B_1|$ distribution. The dipole coil with end-capacitors is of the smallest mean value and the largest CoV of the B_1^+ distribution, whereas the open-ended dipole coil exhibits the largest mean($|B_1^+|$) and the smallest CoV($|B_1^+|$) of the three considered cases. The field parameters of the coil

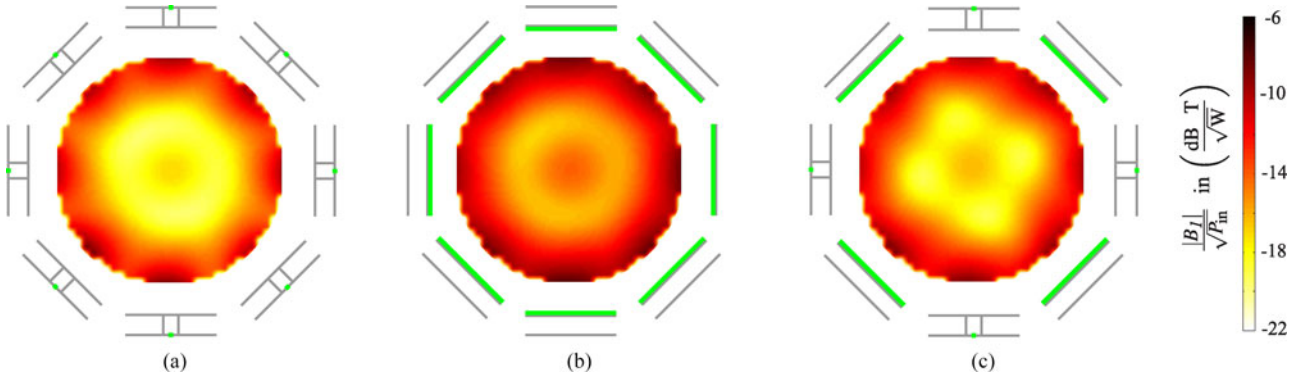

Fig. 4. Measured absolute magnetic field distributions on the transverse cut for the different coil setups: (a) an eight-channel coil based on dipole elements with end-capacitors, (b) an eight-channel coil based on open-ended dipole elements, and (c) an eight-channel coil based on an alternate combination of the aforementioned two dipole elements. The displayed distributions are normalized to the square root of the total delivered power into the coil.

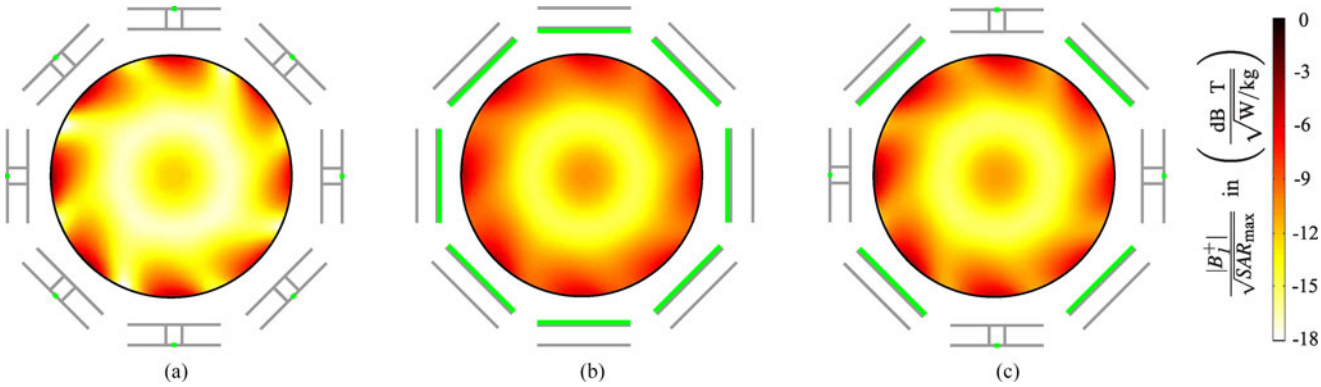

Fig. 5. Simulated $|B_1^+|$ distributions on the transverse cut of the proposed dipole coils: (a) an eight-channel coil based on dipole elements with end-capacitors; (b) an eight-channel coil based on open-ended dipole elements; and (c) an eight-channel coil based on an alternate combination of the aforementioned two dipole elements. The corresponding $|B_1^+|$ distributions are normalized to square root of the peak SAR inside phantom and plotted in dB.

TABLE III
SIMULATED FIELD PARAMETERS OF THE CONSIDERED DIPOLE COILS

Type of Coil	mean $\left(\frac{\lvert B_1^+\rvert}{\sqrt{SAR_{\max}}}\right)$	CoV $\left(\frac{\lvert B_1^+\rvert}{\sqrt{SAR_{\max}}}\right)$
CASE 1: End-Capacitor Element	0.255 $\left[\frac{\mu\mathrm{T}}{\sqrt{\mathrm{W/kg}}}\right]$	0.390
CASE 2: Open-Ended Element	0.321 $\left[\frac{\mu\mathrm{T}}{\sqrt{\mathrm{W/kg}}}\right]$	0.273
CASE 3: Combination of 1 and 2	0.275 $\left[\frac{\mu\mathrm{T}}{\sqrt{\mathrm{W/kg}}}\right]$	0.307

with combined dipole elements fall between the other two cases.

D. Absolute B_1^+ Maps

In addition to the near-field measurement, the absolute B_1^+ maps of the proposed multichannel coils with different dipole elements are acquired with the method presented in [27] in a 7 T MRI scanner (Magnetom 7 T, Siemens Healthcare).

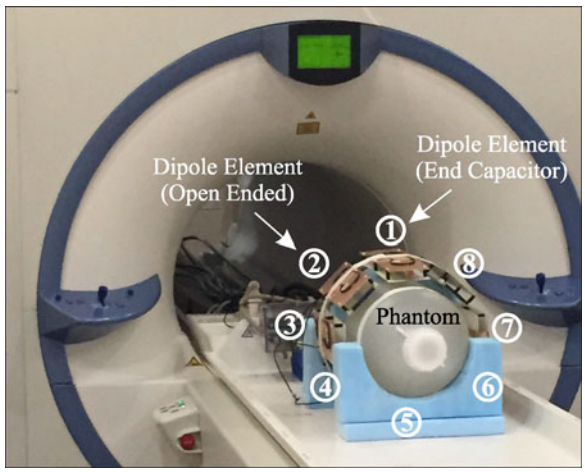

Fig. 6. Eight-channel dipole coil with combined elements loaded with a cylindrical phantom positioned on the patient table of an MRI scanner.

1) Measurement Setup: As shown in Fig. 6, the eight-channel dipole coil with combined elements is loaded with a cylindrical phantom ($\epsilon_r \approx 45$, $\sigma_e \approx 0.8$ S/m, $d = 21$ cm) and positioned on the patient table of a 7 T MRI scanner. The

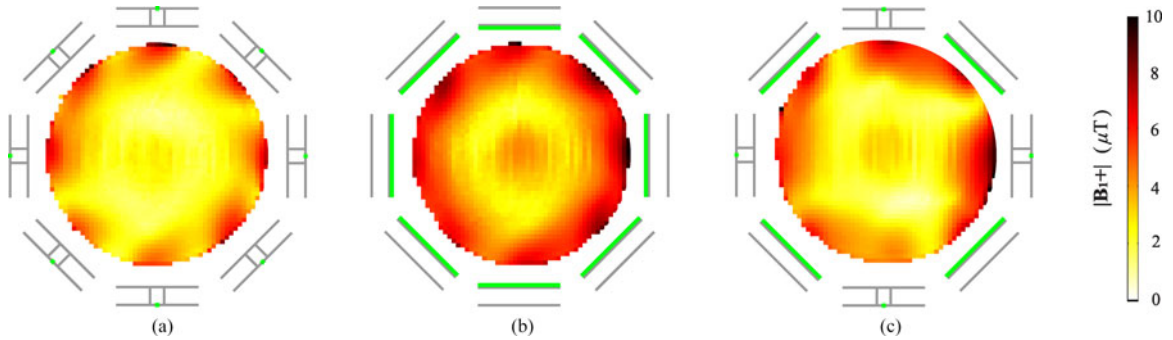

Fig. 7. Acquired absolute transverse B_1^+ maps for different dipole coils: (a) an eight-channel coil based on dipole elements with end-capacitors; (b) an eight-channel coil based on open-ended dipole elements; and (c) an eight-channel coil based on an alternate combination of the aforementioned two dipole elements.

coil elements are fed with 45° phase lag to each other in order to excite the first-order CP+ mode. The peak power applied on each channel is 40 W with 1 ms duration. Including the losses in the RF cables, coil matching network, Tx/Rx switches, etc., the available power that reaches the coil element is less than the applied power. Fig. 6 displays the particular case with combined coil elements, it should be noted that the same measurement setup is applied for the other two cases.

2) Results and Discussion: The absolute B_1^+ maps on the transverse plane of the phantom are compared for different dipole coil arrangements:

1) an eight-channel coil based on dipole elements with end-capacitors,
2) an eight-channel coil based on open-ended dipole elements, and
3) an eight-channel coil based on an alternating combination of the aforementioned two dipole elements.

From Fig. 7(b), it can be seen that the field strength in the region between the coil elements with end-capacitors is considerably lower compared to the primary field excited by the dipole coil, whereas the coil with open-ended elements exhibits an extended field distribution, which significantly improves the field strength in the regions between the neighboring elements. Additionally, the overall field penetration depth of the open-ended scenario is considerably increased as well, indicated by the more obvious "central-brightening" [cf. Fig. 7(b)]. The dipole coil with combined elements reveals an "intermediate" B_1^+ distribution, which falls between the aforementioned two cases. Compared to the end-capacitor scenario, the field strength between the coil elements as well as the field penetration are enhanced for the case using alternating combination of dipole elements. However, the improvement is not as significant as the one achieved with open-ended scenario. The asymmetry of the absolute B_1^+ maps is probably caused by the impurity of the CP+ mode due to the inaccurate relative phase lag between the coil elements. Different matching levels for individual elements and imperfect alignment around the phantom could also aggravate the asymmetry of the B_1^+ distributions.

IV. Coupling Investigation of Eight-Channel RF Coil Based on Different Dipole Elements

Besides the magnetic field distribution, the coupling effect between the coil elements of a multichannel RF coil is another important parameter in the coil design and could significantly influence the coil performance. In this section, the coupling characteristics of the proposed RF coils with different dipole elements are compared by means of the scattering parameters between directly adjacent dipole elements, since these values are the most critical ones.

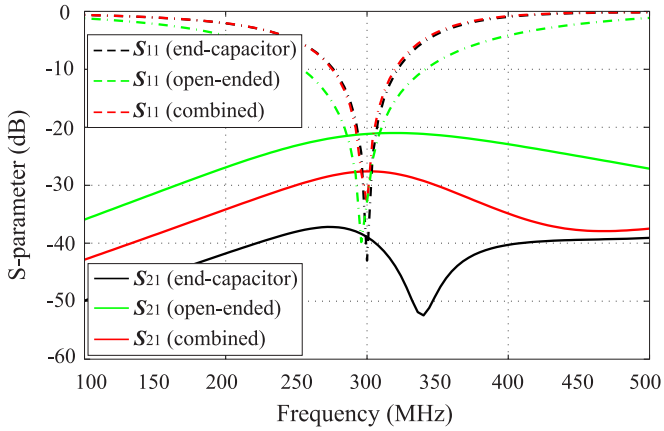

Fig. 8. Simulated S-parameters for the different coil setups depicted in Fig. 2. For each case, one of the dipole elements with the port number 1 is excited with the remaining ports being terminated by 50 Ω loads.

A. Full-Wave Simulation

The coil arrangement for the investigation of coupling characteristics of the different coil setups remains unchanged as depicted in Fig. 2. For each case one of the dipole elements with the port number 1 [cf. Fig. 2(f)] is excited with the remaining adjacent elements being terminated by 50 Ω loads. Normally, the neighboring elements present the strongest coupling due to proximity ("worst-case"). Fig. 8 compares the S-parameters of two directly adjacent elements (with port numbers 1 and 2) for the different coil setups. With appropriate matching networks, more than 35 dB return loss is achieved for all the dipole coils. As expected, the dipole element with end-capacitors achieves a lowest coupling level to the neighboring element of around −38 dB at 300 MHz. Through the extended field distribution the adjacent open-ended dipole elements couple to each other more strongly [cf. Fig. 2(b)], and thus leading to the highest coupling level for the three considered cases ($S_{21} = -21$ dB).

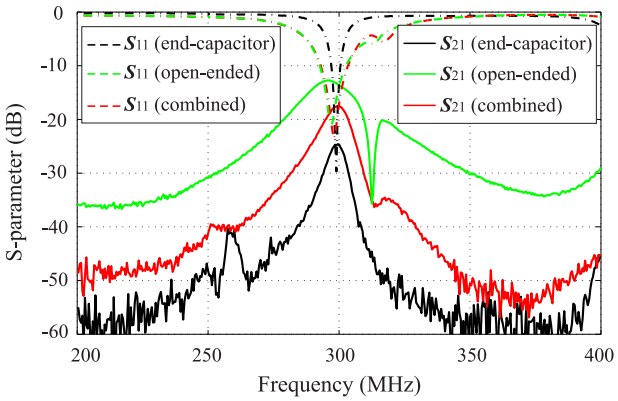

Fig. 9. Measured S-parameters for different coil arrangements as depicted in Fig. 2. For each case the reflection coefficient of the dipole element with the port number 1, as well as the transmission coefficient between port 1 and 2, are measured with the remaining ports being terminated by 50 Ω loads.

As a compromise of the other two scenarios, the dipole coil with combined elements reveals an intermediate S_{21} with a value of -28 dB, which falls between the other two cases.

B. Experimental Validation

The S-parameters of two directly adjacent elements in Fig. 3 are measured with a two-port network analyzer for the different coil setups. With the proper matching networks, more than 20 dB return loss is achieved for all the coil elements in the different coil setups. As shown in Fig. 9, the coil with end-capacitors reveals a most promising decoupling between the neighboring elements, indicated by the smallest S_{21} of -25 dB at 300 MHz. The coil consisting of open-ended elements exhibits the highest coupling level around -14 dB due to the broader and overlapped field distributions inside phantom. The coupling level of the coil with combined elements falls in between the aforementioned two scenarios, showing an intermediate S_{21} with a value of -18 dB. Generally, an excellent agreement between the simulation and measurement results is observed.

V. Conclusion

The magnetic field distribution and coupling characteristics of a multichannel RF coil consisting of different dipole elements for 7 T MRI are investigated. Two types of dipole elements are considered here: the meandered dipole element with lumped-element connection to the RF shield (end-capacitor scenario), and through an electromagnetic field-based coupling to the RF shield (open-ended scenario). It has been shown that the open-ended dipole coil exhibits a better magnetic field distribution, whereas the dipole coil with end-capacitors achieves a sufficient decoupling between the neighboring elements. Hence, a coil setup which combines the aforementioned two types of dipole elements is proposed. By nesting the open-ended dipole elements in between the ones with end-capacitors, the magnetic field distribution is improved in comparison to the dipole coil consisting only of the elements with end-capacitors, and additionally, the adjacent element are less coupled to each other in comparison to the dipole coil consisting only of the open-ended elements. Here we demonstrated the feasibility to achieve a compromise between field distribution and coupling behavior by combining different dipole coil elements. The presented investigation is based on full-wave simulations and corresponding measurements, which match to each other very well. In addition to the near-field measurement, the eight-channel coil with different dipole elements are tested in a 7 T MRI scanner, which validated the proposed approach. The arrangement of different dipole elements (in terms of number and position) shall be optimized depending on specific applications (various body regions), which will be investigated in the future.

Acknowledgment

The authors would like to thank H. H. Quick, O. Kraff, S. Orzada, and S. Brunheim, from Erwin L. Hahn Institute for Magnetic Resonance Imaging, for their support and help at the 7 T MRI scanner.

References

[1] M. E. Ladd, "High-field-strength magnetic resonance: Potential and limits," *Top Magn. Reson. Imag.*, vol. 18, pp. 139–152, 2007.
[2] E. Moser *et al.*, "7-T MR from research to clinical applications?" *NMR Biomed.*, vol. 25, pp. 695–716, 2012.
[3] P.-M. Robitaille and L. J. Berliner, *Ultra High Field Magnetic Resonance Imaging*, vol. 26 (Biological Magnetic Resonance). New York, NY, USA: Springer, 2006.
[4] D. G. Norris, "High field human imaging," *J. Magn. Reson. Imag.*, vol. 18, no. 5, pp. 519–529, 2003.
[5] R. R. Regatte and M. E. Schweitzer, "Ultra-high-field MRI of the musculoskeletal system at 7.0T," *J. Magn. Reson. Imag.*, vol. 25, no. 2, pp. 262–269, 2007.
[6] K. Ugurbil *et al.*, "Ultrahigh field magnetic resonance imaging and spectroscopy," *Magn. Reson. Imag.*, vol. 21, no. 10, pp. 1263–1281, 2003.
[7] P.-F. Van de Moortele *et al.*, "B_1 destructive to interferences and spatial phase patterns at 7 T with head transceiver array coil," *Magn. Reson. Med.*, vol. 54, pp. 1503–1518, 2005.
[8] J. T. Vaughan *et al.*, "7T vs. 4T: RF power, homogeneity, and signal-to-noise comparison in head images," *Magn. Reson. Med.*, vol. 46, no. 1, pp. 24–30, 2001.
[9] J. T. Vaughan and J. R. Griffiths, Eds., *RF Coils for MRI*. Hoboken, NJ, USA: Wiley, Aug. 2012.
[10] W. Mao *et al.*, "Exploring the limits of RF shimming for high-field MRI of the human head," *Magn. Reson. Med.*, vol. 56, no. 4, pp. 918–922, 2006.
[11] S. Sengupta *et al.*, "Dynamic B_0 shimming at 7 T," *Magn. Reson. Imag.*, vol. 29, no. 4, pp. 483–496, 2011.
[12] B. van den Bergen *et al.*, "SAR and power implications of different RF shimming strategies in the pelvis for 7T MRI," *J. Magn. Reson. Imag.*, vol. 30, no. 1, pp. 194–202, 2009.
[13] J. T. Vaughan *et al.*, "Whole-body imaging at 7T: Preliminary results," *Magn. Reson. Med.*, vol. 61, no. 1, pp. 244–248, 2009.
[14] A. Raaijmakers *et al.*, "Why do dipole antennas work? A comparison to loop coils as a function of element size," in *Proc. 22nd Int. Soc. MRM*, Milan, Italy, May 10–16, 2014, p. 4887.
[15] J. T. Vaughan *et al.*, "Efficient high-frequency body coil for high-field MRI," *Magn. Reson. Med.*, vol. 52, pp. 851–859, 2004.
[16] G. Adriany *et al.*, "Transmit and receive transmission line arrays for 7 Tesla parallel imaging," *Magn. Reson. Med.*, vol. 53, pp. 434–445, 2005.
[17] D. O. Brunner *et al.*, "A symmetrically fed microstrip coil array for 7T," in *Proc. 15th Int. Soc. MRM Joint Annu. Meet.*, 2007, p. 448.
[18] G. Adriany *et al.*, "A geometrically adjustable 16-channel transmit/receive transmission line array for improved RF efficiency and parallel imaging performance at 7 Tesla," *Magn. Reson. Med.*, vol. 59, pp. 590–597, 2008.
[19] S. Orzada *et al.*, "16-channel Tx/Rx body coil for RF shimming with selected Cp modes at 7T," in *Proc. 18th Sci. Meet. Int. Soc. MRM*, Stockholm, Sweden, May 1–7, 2010, p. 50.
[20] A. J. E. Raaijmakers *et al.*, "Design of a radiative surface coil array element at 7 T: The single-side adapted dipole antenna," *Magn. Reson. Med.*, vol. 66, pp. 1488–1497, 2011.

[21] Z. Chen *et al.*, "Coupling investigation of different RF coil elements for 7-Tesla magnetic resonance imaging based on characteristic mode analysis," in *Proc. IEEE MTT-S Int. Microw. Symp. Dig.*, Tampa Bay, FL, USA, Jun. 1–6, 2014, pp. 1–4.
[22] R. F. Harrington and J. R. Mautz, "Theory of characteristic modes for conducting bodies," *IEEE Trans. Antennas Propag.*, vol. AP-19, no. 5, pp. 622–628, Sep. 1971.
[23] S. Orzada *et al.*, "A novel 7 T microstrip element using meanders to enhance decoupling," in *16th Proc. Int. Soc. MRM*, Toronto, ON, Canada, May 3–9, 2008, p. 2979.
[24] Z. Chen *et al.*, "Dipole RF element for 7 tesla magnetic resonance imaging with minimized SAR," in *Proc. 7th Eur. Antennas Propag. Conf.*, Gothenburg, Sweden, Apr. 8–12, 2013, pp. 1775–1778.
[25] D. I. Hoult *et al.*, "Quadrature detection in the laboratory frame," *Magn. Reson. Med.*, vol. 1, no. 3, pp. 339–353, Sep. 1984.
[26] G. H. Glover *et al.*, "Comparison of linear and circular polarization for magnetic resonance imaging," *J. Magn. Reson.*, vol. 64, pp. 255–270, 1985.
[27] S. Brunheim *et al.*, "Combining B1 mapping with TIAMO for fast and accurate multi-channel RF shimming in 7 Tesla body MRI," in *Intl. Soc. Magn. Reson. Med. 24th Ann. Meet. Exhib.*, Singapore, May 7–13, 2016, p. 0936.

Zhichao Chen (S'13) received the B.S. and M.S. degrees in electrical and electronic engineering, in 2009 and 2012, respectively, from the University of DuisburgEssen, Duisburg, Germany, where he is currently working toward the Ph.D. degree in electrical engineering. His general research interests include array antennas, metamaterials and associated applications, numerical simulation methods, and electromagnetic theory. His current research is focused on the development of RF components for magnetic-resonance imaging systems, especially for ultrahigh field strength.

Klaus Solbach was born in Witten, Germany, in 1951. He received the Dipl.-Ing. degree in electrical engineering from Rheinisch-Westflische Technische Hochschule Aachen University, Aachen, Germany, in 1974, and the Dr.-Ing. degree from the University of Duisburg, Duisburg, Germany, in 1979.

From 1975 to 1980, he was with the University of Duisburg, as a Researcher, where he was involved in the field of integrated dielectric image line circuits in the millimeter-wave frequency range. In 1981, he joined the Millimeter Wave Research Laboratory, AEG-Telefunken, Ulm, Germany, where he designed receive/transmit circuits and antennas for millimeter-wave radar and communications equipment. After joining the Radar Systems Group, Daimler-Benz Aerospace, in 1984, he got engaged in the design and production of microwave subsystems for ground-based and airborne radar, electronic warfare (EW), and communication systems, including phased-array and active phased-array antenna systems. He was the Manager of the RF-and-Antenna-Subsystems Department, Daimler-Benz Aerospace, Ulm, Germany. In 1997, he joined the faculty of the University of Duisburg, as the Chair for RF and Microwave Technology. After serving as the Vice-Dean of the Department of Electrical Engineering and the Dean of the newly founded Faculty of Engineering, he then served as the Vice-Rector of the newly merged University DuisburgEssen until the end of 2006. He has authored or coauthored more than 200 national and international papers, conference contributions, book chapters, and patent applications.

Dr.-Ing. Solbach was the Chairman of the VDE-ITG Fachausschuss "Antennen," the Executive Secretary of the Institut für Mikrowellen-und Antennentechnik (IMA), and the Chair of the IEEE German AP/MTT Joint Chapter. He has been a Member of the Editorial Board of the IEEE TRANSACTIONS ON MICROWAVE THEORY AND TECHNIQUES. He has been a Member of a number of Technical Program Committees of national and European scientific conferences. In 2007, he was the General Chair of the international ITG-Conference on Antennas INICA2007, Munich, Germany, and in 2009, he was the General Chair of the European Conference on Antennas and Propagation, Berlin, Germany.

Daniel Erni (S'88–M'93) received the Diploma degree in electrical engineering from the University of Applied Sciences in Rapperswil (HSR), Rapperswil-Jona, Switzerland, in 1986, and the Diploma degree in electrical engineering and Ph.D. degree in laser physics from ETH Zürich, Zürich, Switzerland, in 1990 and 1996, respectively.

Since 1990, he has been with the Laboratory for Electromagnetic Fields and Microwave Electronics, ETH Zürich. From 1995 to 2006, he was the Founder and Head of the Communication Photonics Group, ETH Zürich. Since October 2006, he has been a Full Professor for general and theoretical electrical engineering with the University of DuisburgEssen, Duisburg, Germany. His current research interests include advanced data transmission schemes (i.e., optical multiple input multiple output) in board-level optical interconnects, optical on-chip interconnects, ultra-dense integrated optics, nanophotonics, plasmonics, quantum optics, electromagnetic and optical metamaterials, and applied electromagnetics (cf. electromagnetic metamaterials for applications in magnetic resonance imaging). On the system level, he has pioneered the introduction of numerical structural optimization into dense integrated optics device design. His further research interests include science and technology studies, as well as the history and philosophy of science with a distinct focus on the epistemology in engineering sciences.

Dr. Erni is a Fellow of the Electromagnetics Academy. He is a Member of the Center for Nanointegration Duisburg-Essen, an Associate Member of the Swiss Electromagnetics Research Centre, and also a Member of the Swiss Physical Society, the German Physical Society (DPG), and the Optical Society of America.

Andreas Rennings (M'01) received the Dipl.-Ing. and Dr.-Ing. degrees in electrical engineering from the University of Duisburg-Essen, Essen, Germany, in 2000 and 2008, respectively. He carried out his diploma work at the Microwave Electronics Laboratory, University of California at Los Angeles, Los Angeles, CA, USA.

From 2006 to 2008, he was with IMST GmbH in Kamp-Lintfort, Germany, where he worked as an RF engineer. Since then, he is a Senior Scientist in the Laboratory for General and Theoretical Electrical Engineering, University of Duisburg-Essen, leading several research projects. His general research interests include all aspects of theoretical and applied electromagnetics, currently with a focus on medical applications. He has authored and co-authored more than 80 conference and journal papers and 1 book chapter and filed 8 patents.

Mr. Rennings received several awards, including the second price within the student paper competition of the 2005 IEEE Antennas and Propagation Society International Symposium and the VDE-Promotionspreis 2009 for his doctoral thesis.